ORIGINAL RESEARCH ARTICLE

Influence of Residual Stress on Mechanical and Tribology Behaviors of Calcium-Phosphate Coating on Commercially Pure Titanium via Integrated Electrospinning and Rapid Heating and Cooling Process

Khashayar Saei Hamedani, Minoo Yadi, and Hamid Esfahani

This study focuses on the role of residual stress in the tribological behavior of calcium-phosphate (CaP) coating on titanium (Ti) substrate. The CaP coating was applied using an integrated electrospinning and rapid heating and cooling (EMRHC) process. The residual stress over half and full done EMRHC process was measured by x-ray method. The substrate and coatings were characterized using a field emission scanning electron microscope equipped with the energy-dispersive spectroscope, Vicker's microhardness, atomic force microscopy, and x-ray diffractometer techniques. It was found that the preliminary hydroxyapatite on the Ti substrate was exchanged with α-TCP, CaO, TiO$_2$, CaTiO$_3$, and Ti$_5$P$_3$ over the EMRHC process. The results also showed that the tensile $+ 591 \pm 89$ and compressive $- 189 \pm 42$ MPa residual stress remained on the surface over the half and full done EMRHC process, respectively. The hardness, Young module, and ultimate tensile strength of both samples were enhanced significantly by the EMRHC process. The tribology of samples was comprehensibly evaluated in a dry and simulated body fluid solution. The CaP coating prepared by the full-EMRHC process showed the lowest wear rates in comparison with the others due to the compressive residual stress. The coefficient of friction of CPTi coated by EMRHC was significantly reduced when exposed to the SBF solution. Our findings revealed that EMRHC is a promising method to fabricate the Ti implant with higher mechanical properties.

1. Introduction

Titanium and its alloys are widely used in human orthopedic implants because of their biocompatibility, low elastic modulus, and the high strength-per-weight ratio (Ref 1, 2). However, titanium has a limited ability to induce and integrate with the alive bone resulting in implant loosening and implant failure (Ref 3-5). Also, titanium is susceptible to corrosion in the human body which impedes its clinical application (Ref 6). Furthermore, the poor wear resistance and a high coefficient of friction of titanium are the major weakness that needs solve before implantation (Ref 7).

The wear debris causes inflammatory and immunological responses (Ref 8). Moreover, serious problems may be occurred with releasing the debris from the titanium implants such as blood clotting, death of surrounding tissues, and moving giant cells into debris disrupting the host tissue (Ref 9, 10). Therefore, an excellent wear resistance coating on the titanium surface, on the one hand, and a coating with an appropriate topography, on the other hand, is necessary because the worn debris may be accumulated by the textures of the coating, and thus, the wear rate decreases (Ref 11). It is worth mentioning that the mismatched Young's modulus of the coating results in the symptoms as those issued by poor wear resistance (Ref 8).

Surface modification by the hard components (e.g., carbides, nitrides, borides) may be useful to improve the hardness and wear resistance of titanium (Ref 7); however, they cannot enhance the bioactivity of the surface. Therefore, to overcome the mentioned problems, a bioactive and protective coating should be applied on the titanium surface (Ref 12-14). Several methods have been developed to deposit the bioactive coatings on the titanium substrate such as pulsed laser deposition (Ref 15), sputter deposition (Ref 16), plasma spray (Ref 17), electrophoretic (Ref 18), suspension spray (Ref 19), sol-gel (Ref 20), thermal spray (Ref 21), laser treatment (Ref 22), and ion beam deposition (Ref 23).

The surface modification of titanium to improve the wear resistance via the mentioned method has the disadvantages such as being too thin to stand with the loads, deformation of the

Khashayar Saei Hamedani, Minoo Yadi, and **Hamid Esfahani**, Department of Materials Engineering, Faculty of Engineering, Bu-Ali Sina University, Hamedan, Iran. Contact e-mail: h.esfahani@basu.ac.ir.

workpiece, and long processing time (Ref 7). In recent years, different coating methods have been employed to create the bioactive coating, namely the electrospinning method. With the electrospinning process, a hybrid polymer-ceramic coating with a variety of compositions at the nanoscale can be obtained (Ref 24). Hydroxyapatite (HA) as the main mineral in vertebrate bone and tooth tissues (Ref 25) can be easily deposited on the metallic and ceramic substrates by the electrospinning method (Ref 26). The brittleness, low flexural and mechanical properties, and low bonding with titanium substrate tend to limit the use of single-phase HA (Ref 4). The reinforcement process has been suggested to improve the mechanical characteristics of HA coatings on the titanium substrate (Ref 27). However, the reinforcing agents (e.g., Al_2O_3, ZrO_2, CNT, and TiO_2) also are exposed to problems issued by releasing debris (Ref 28). We need a process that first of all, maintains biocompatibility, and then enhances the chemical bonding of the HA with the titanium substrate. The heating process is the most effective parameter affecting the crystallization, microstructure, and mechanical properties of the HA (Ref 4). In this study, we applied the rapid heating and cooling process on the deposited HA nanoparticles (NPs) on the commercially pure titanium (CPTi) via the electrospinning method. In our previous work (Ref 29), we presented the successful corrosion resistance, bioactivity, and cytocompatibility of electrospinning and rapid heating and cooling (EMRHC) coatings on the CPTi. However, we believe that internal stress might have existed in the titanium substrate over the EMRHC process which influences the adhesion and subsequently the wear resistance of coatings. In fact, it is difficult of producing a coating without residual stress (Ref 30). The tensile residual stress vertically to the direction of the coating can apart the coating from the substrate (Ref 31). Chang et al. (Ref 32) found that the residual stress of a steel substrate might be reduced with a decrease in the grain size of the TiN film, it cannot completely be vanished. Nimkerdphol et al. (Ref 33) observed the compressive residual stress in the heat-treated HA coatings on the CPTi substrate. They reported that the melting of CaP particles was responsible for the distribution of stress around the particles of coating.

The residual stress may be inherently induced in the rapid heating and cooling process because of the different thermal properties of the ceramic coatings and metallic substrate. Also, the complicated chemical relations between HA and Ti affect the residual stress (Ref 34). The temperature of the substrate, the thickness of the coating, the diversity of ceramic compounds in the coating, and the rate of cooling are the main factors that affect the residual stress (Ref 35). The tensile residual stress causes to initiate cracks, while the compressive residual stresses cause to delay the crack initiation (Ref 36).

To date, several research works have been conducted on the development of HA coating on titanium substrate, and investigation on their residual stresses (Ref 37). In our previous experiences with the laser treatment (Ref 22), we found that the HA NPs embedded inside the polyvinylidene (PVP) fibrous mats can be decomposed via the laser treatment, and by regulating the laser traveling speed and laser beam diameter, the heat input value is changed, and therefore, the diversity of amounts and types of α- $Ca_3(PO_4)_2$, $CaTiO_3$, $Ca_4P_2O_9$, $Ca_8H_2(PO_4)_6.5H_2O$ phases can be achieved on the CPTi substrate. In fact, the EMRHC process is a simple process that employs the rapid heating up and cooling down steps in heat treatment methods like laser treatment, but it does not need expensive and complex equipment. This study has considerable

efforts to explore the residual stress developed during the novel EMRHC method applied at half done (H-EMRHC) and full done (F-EMRHC) process. Among the methods, the x-ray diffraction method as a nondestructive method was applied to find the complete in-plane stress distribution (Ref 34). Furthermore, the mechanical and wear properties of EMRHC coatings were studied with regard to residual stress. Also, the wear properties of EMRHC coatings in the simulated body fluid (SBF) were studied as one essential requirement for an orthopedic implant.

2. Materials and Methods

2.1 Sample Preparation by EMRHC Process

The commercially pure titanium (CPTi-Grade 2) as the substrate was purchased. The surface of the samples ($0.1 \times 1 \times 2$ cm^3) was prepared by sandpaper No.2000, polished, and then cleaned with ethanol to remove any potential contaminants. HA nanoparticles (NPs) were synthesized via the wet chemical precipitation method (Ref 38). The EMRHC process was carried out in two steps, involving electrospun masking and heat treatment. In the first step, the electrospinning solution was prepared by blending HA NPs with polyvinylidene (PVP ($C_6H_9NO)_n$, Merck 107443) in ethanol, with a mass ratio of 0.17 (wt.%/wt.%). A stainless-steel needle, 20 kV DC high voltage, 15 cm distance from the surface of the specimen to the needle, and 0.2 mL h^{-1} feeding rate were applied to create the electrospun mask on the CPTi samples. In the second step, the masked samples were heat-treated in an air atmospheric furnace. The sample was soaked at 400 °C for 5 min, then cooled rapidly in the air atmosphere to achieve the H-EMRHC coating. This process was repeated at 700 °C to achieve the F-EMRHC coating. A typical photo of the CPTi specimen before and after the F-EMRHC process is shown in Fig. 1(a).

2.2 Characterization

The morphology was studied using a scanning electron microscope (SEM, JEOL-JSM 840 A, Japan) and a field emission scanning electron microscope (FESEM, T-scan MIRA3 equipped with EDS analyzer). To measure the sizes, ImageJ (ImageJ 1.38x, NIH, Bethesda, MD, USA) was employed. Phase detection was performed by x-ray diffractometer (XRD; device model; Philips PW1730 by kα Cu, $\lambda = 0.154$ nm). X'Pert HighScore Plus software (ver. 2.2b, 2.2.2) was also applied for further investigation. The surface topography of samples was evaluated by an atomic force microscope (AFM). Surface roughness values were assessed by the Nanosurf Mobile S software. The wettability was studied by monitoring the water contact angle (WCA) of a water droplet during 120 s of contact. The average values and standard deviation were calculated with three repetitions of the tests to ensure reproducibility. To evaluate the quality of the adhesion of the coating, a Rockwell-C adhesion test developed by the Union of German Engineers (Verein Deutscher Ingenieure, VDI) (Ref 39) was used. To do this, a load of 980 Kgf for 30 seconds was applied, and then the effect of the indenter was compared to classification HF1 to HF6 according to the level of cracking and coating delamination around the indent. The Microhardness Vickers tester with a load of 25 g f^{-1} was used to
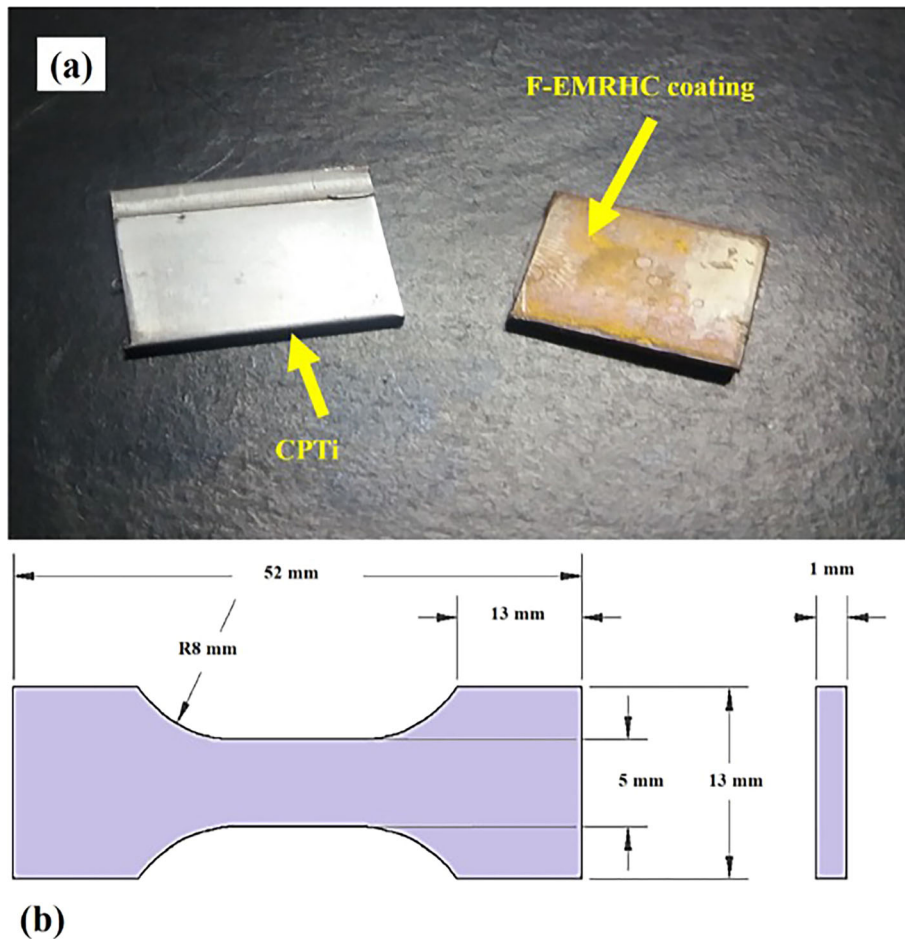
Fig. 1. (a) A photo of the CPTi specimen before and after the F-EMRHC process, and (b) schematic presentation for size of the tensile test specimen.

measure the hardness of the samples. To evaluate the mechanical properties, the pure and modified CPTi samples were prepared based on the size and dimension as presented in Fig. 1(b). The tensile test was performed by a device model SANTAM 5 T with the following parameters: measuring length 36 mm and crosshead speed 2 mm min^{-1}. To ensure the reputability, each sample was analyzed three times, and the average was reported. To evaluate the wear behavior, the pure and modified CPTi samples were provided ($0.1 \times 1 \times 2$ cm^3) and tested in dry and wet conditions. For dry condition, the wear evaluation was carried out by the pin-on-disk method according to the guidelines of the ASTM G99 standard. The pin was made from stainless-steel 52,100. The normal force (F_n) of 5 N in the friction mode was applied. The rate (r) of 0.02 m s^{-1} was used. The total covered distance was set at 100 m. The friction coefficient (COF) was monitored by a load cell attached to the computer, and weight loss was measured by a high-accuracy balance. The samples were carefully washed with acetone before weighing. To measure the depth of wear, the cross view dimension of the track was analyzed by a surface profilometer (Nano Pajouhan Raga Co. 50.10. S). For the wet condition, first, the SBF solution was provided according to the procedure described by Kokubo (Ref 40). The pin-on-disk wear mode was performed in 50 mL of the fresh SBF solution. The other wear parameters (force, distance, and rate) and measurement methods were as same as those mentioned above. The

debris released from the samples in both conditions was collected for the microstructure analysis.

2.3 Residual Stress Measurement

The residual stress generated by the EMRHC process was precisely evaluated by means of the XRD-sin$^2(\psi)$ technique (Ref 41). To do this, the samples ($0.1 \times 1 \times 2$ cm^3) coated by the EMRHC process without further treatment were analyzed by the XRD device. The XRD device model; Philips PW1730 by kα Cu, $\lambda = 0.154$ nm was applied to several scanning by x-ray on the normal surface at $\psi = 0$ °. The linear regression analyzing the $d_{hkl} - \sin^2(\psi)$, the residual stress (σ) was achieved. The X'Pert HighScore Plus software (ver. 2.2b, 2.2.2) was applied to calculate the d_{hkl} and $\sin^2(\psi)$ for a known 2θ.

3. Results and Discussion

3.1 Morphology and Phase Study of the EMRHC Coatings

EMRHC process is capable to modify the metallic surface for use in biomedical applications (Ref 29). The surface microstructures of pure CPTi and EMRHC-coated CPTi are presented in Fig. 2. With applying the electrospun PVP/HA
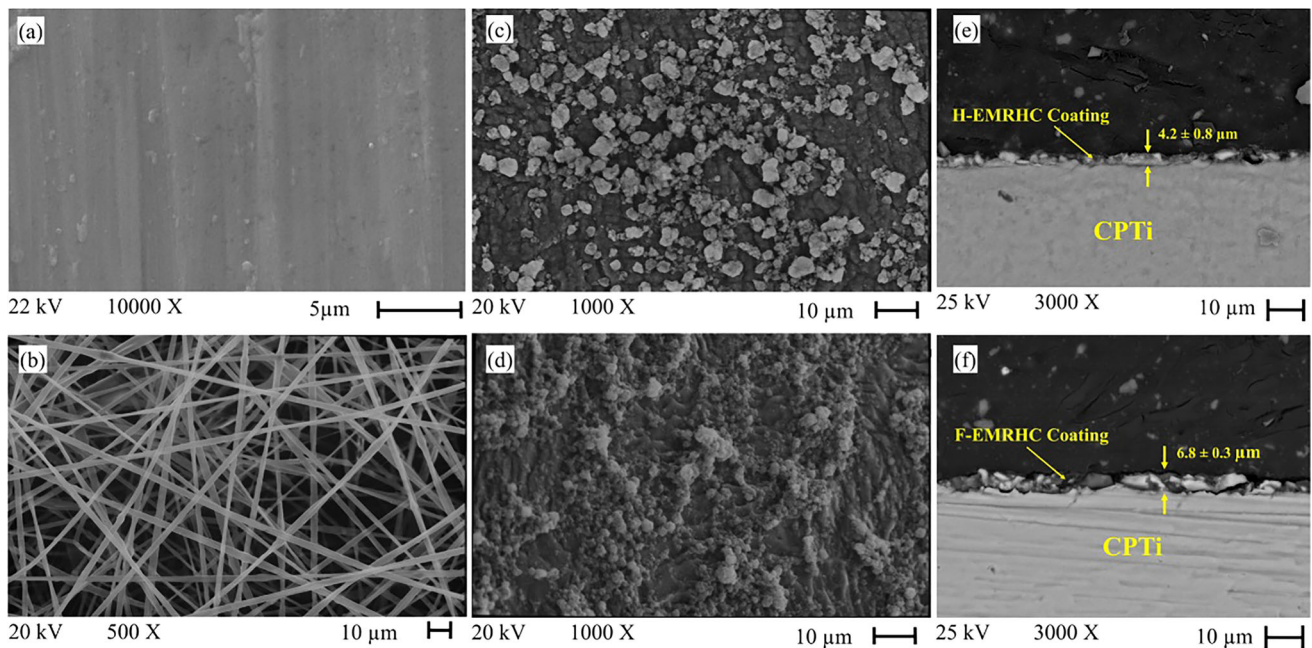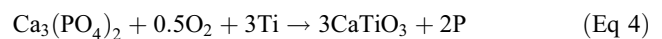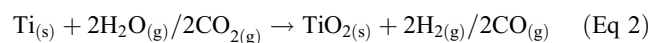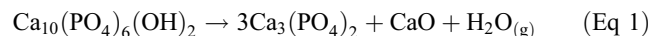
Fig. 2. SEM images of surface of (a) CPTi, (b) electrospun PVP/HA mask on the CPTi, (c) H-EMRHC-coated CPTi, and (d) F-EMRHC-coated CPTi, and cross view SEM images of half (e) and full done (f) EMRHC-coated CPTi.

mask, the morphology of the CPTi surface was changed drastically. During the heat treatment step, the electrospun mask was subjected to the removal of ethanol, acetate, nitrate, PVP, the reaction of coating with CPTi substrate, as well as the formation of the crystalline HA particles. To understand the potential of heat input on mentioned developments, the thermal process was performed at two temperatures, 400 and 700 °C for 5 minutes. In our previous study (Ref 29), we found that the heat treatment at 400 °C tends to the incomplete chemical reaction between Ti and CaP top coatings, and in contrast, at 700 °C the full reactions were tack placed. Figure 2(c) and (d) demonstrates the microstructure of H-EMRHC and F-EMRHC coatings. The changes in the nanofibrous morphology are due to the breakdown of PVP. In other words, the rate of breakdown and the rate of crystallization are two key factors that affect the structure and morphology of the coating. The heating process results in the formation of ceramic aggregates due to the breakdown of organic materials and the crystallization and formation of various CaP compounds (Ref 42). The SEM images of EMRHC-coated CPTi demonstrated that these two specimens differ morphologically from each other. By H-EMRHC coating, the particles with a broad distribution size and non-homogeneous distribution were observed, whereas, by F-EMRHC coating, the morphology of ceramic aggregates appeared more continuously with the homogeneous structure on the CPTi surface. It was also found that the thickness of the coating created by the F-EMRHC process ($\sim$ 6.8 μm) was higher than the H-EMRHC coating (($\sim$ 4.2 μm).

The EDS analysis was applied to the EMRHC-coated samples to determine the nature of the coating. The determination of P and Ca peaks, as shown in Fig. 3(a) and (b), confirms the existence of a calcium-phosphate compound on the surface of CPTi. The Ti and O peaks were also observed, and the absence of other elements confirmed the purity of the coating. Moreover, by calculating the atomic percent of elements, it cannot be unequivocally stated that a stoichiometric

HA with an atomic Ca/P ratio of 1.67 was formed, as the HA coating has undergone phase changes due to thermal processing, resulting in phase transformations. Hence, a phase study by XRD analysis was carried out to understand the phase changes during the heat treatment.

The PVP, HA, and Ti are the reactants of the EMRHC process in which the PVP/HA makes the electrospun mask, and Ti creates the substrate. The reactants are exchanged by the products over the heat treatment. The PVP is eliminated at 250-300 °C; therefore, it cannot be considered as the reactants in H-EMRHC and F-EMRHC coatings. The XRD pattern of CPTi and HA NPs as the main reactants is presented in Fig. 4(a). The purity and stoichiometry of HA NPs were confirmed by strong matching with the standard card JCDPS 01-086-1199. The XRD patterns of H-EMRHC and F-EMRHC coatings have been given in the 2θ range of 23-34 ° to compare the consumption of the source with preliminary reactants. It was observed that the amount and crystallinity of HA were reduced by applying the EMRHC process at the higher temperature indicating that more reactions take place between Ti and HA. Briefly, the HA decomposed to $Ca_3(PO_4)_2$ (α-TCP) and CaO according to Eq 1, the H_2O and CO_2 off-gas could oxide the Ti substrate (Eq 2), and then the CaO and TiO_2 reacted to form the $CaTiO_3$ (CTO) based on Eq 3; in addition, the phosphor atoms created beside the CTO could create the Ti_5P_3 (Eq 4-5).

$$Ca_{10}(PO_4)_6(OH)_2 \rightarrow 3Ca_3(PO_4)_2 + CaO + H_2O_{(g)} \quad \text{(Eq 1)}$$

$$Ti_{(s)} + 2H_2O_{(g)}/2CO_{2(g)} \rightarrow TiO_{2(s)} + 2H_{2(g)}/2CO_{(g)} \quad \text{(Eq 2)}$$

$$TiO_{2(s)} + CaO_{(s)} \rightarrow CaTiO_{3(s)} \quad \text{(Eq 3)}$$

$$Ca_3(PO_4)_2 + 0.5O_2 + 3Ti \rightarrow 3CaTiO_3 + 2P \quad \text{(Eq 4)}$$

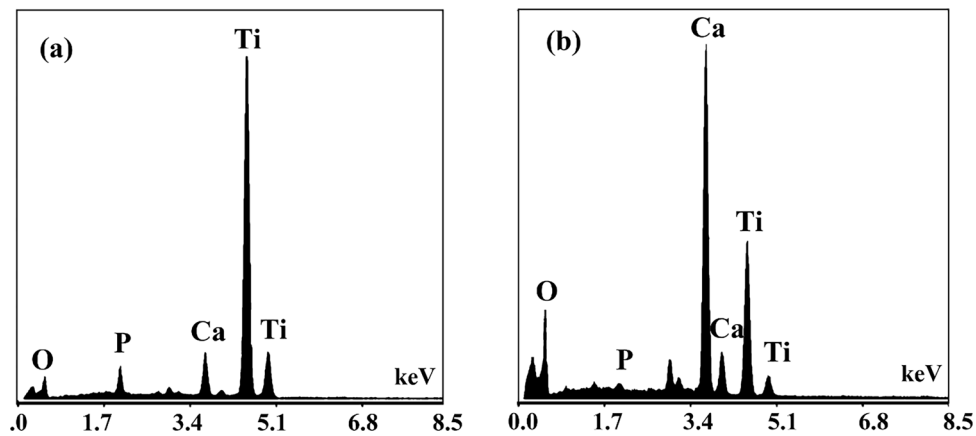$$5Ti + 3P \rightarrow Ti_5P_3 \quad \text{(Eq 5)}$$

Fig. 3. EDS spectra corresponding to the surface of (a) H-EMRHC-coated CPTi, and (b) F-EMRHC-coated CPTi.

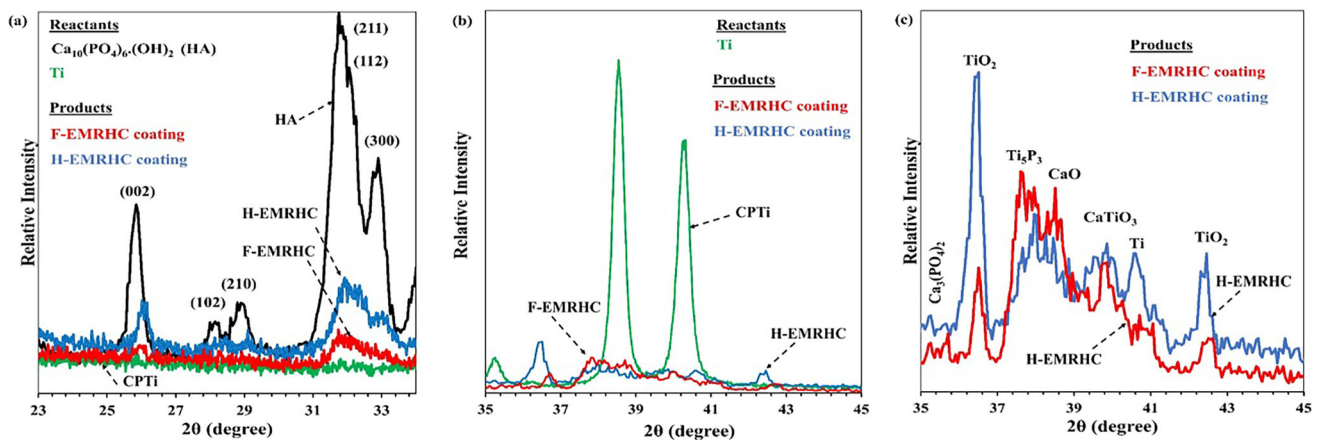**Fig. 4.** XRD patterns of HA NPs, CPTi, H-EMRHC, and F-EMRHC coatings in the range of $2\theta = 23\text{-}34$ º to identify the HA source consumption (a). GIXRD patterns of H-EMRHC coating and F-EMRHC coating comparison with (b) and without (c) XRD pattern of CPTi in the range of $2\theta = 35\text{-}45$ º to identify the formation of the products.

The GIXRD patterns of EMRHC coatings in the range of 2θ range of 35-45 º were compared with the XRD pattern of CPTi to identify the produced phases on top of the CPTi (Fig. 4b). It was found that drastic changes have occurred on the surface of the CPTi over the EMRHC process. To identify the products, the GIXRD patterns of H and F-EMRHC coatings were compared together (Fig. 4c). It was confirmed that the α-TCP (00-029-0359), CaO (01-082-1691), TiO_2 (01-072-1148), CTO (01-075-2099), and Ti_5P_3 (00-045-0888) are the main products of EMRHC process. According to the intensity fraction of TiO_2, it was elucidated that the heat treatment at the higher temperature caused more consumption of TiO_2 and further production of CTO, Ti_5P_3, and α-TCP.

3.2 Characterization of EMRHC Coatings

The morphology studies showed that the ceramic products created the aggregates on the CPTi homogenously attached to the substrate whereas heterogeneously bonded with the Ti. To understand the topography and its effect on the mechanical and wear properties, the CPTi and EMRHC-coated samples were determined by AFM. The topography of the surfaces as shown in Fig. 5 compares the half and full done EMRHC coatings on the CPTi with the surface of untreated CPTi. Also, the roughness parameters (R_a) and (R_q) based on the AFM images

were determined as the amount given in Table 1. The topography of titanium implants has a significant role in biomedical applications especially for cell proliferation and attachment (Ref 43). The results showed that the roughness of the CPTi surface was changed with applying the EMRHC process. The surface roughness was increased after the H-EMRHC process. Both R_a as an average of a set of individual measurements of surface peaks and valleys, also R_q as the root mean square average of the profile height deviations from the mean line, recorded within the evaluation length, revealed that the F-EMRHC coating caused a more smooth surface. As can be seen in AFM micrographs, H-EMRHC coating had more peaks and valleys, which can act as stress concentrators and lead to accelerated wear due to the formation of microcracks and surface fatigue (Ref 44). On the other hand, it is expected that F-EMRHC coating with a smoother surface will have fewer stress concentrators and a more uniform distribution of stresses, resulting in improved wear resistance. Furthermore, surface topography can have a significant impact on wettability.

The wetting properties of a solid surface play a crucial role in various applications inside or expose to the aqueous environment (Ref 45). This property may influence other surface properties, including corrosion and wear resistance. Several factors such as surface roughness, chemical composition, and microstructure significantly affect the wetting behav-
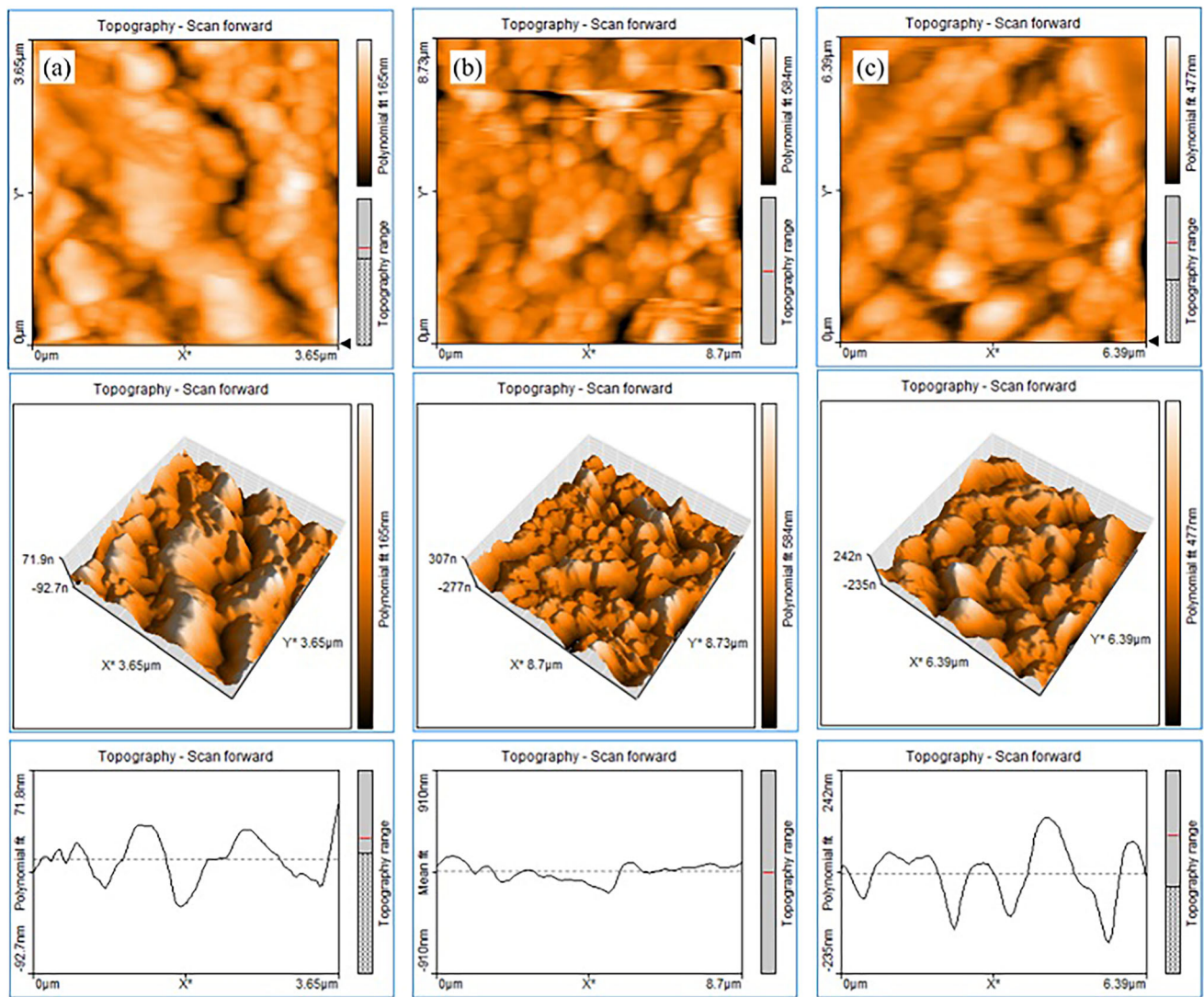
Fig. 5. AFM results of surface profile of (a) CPTi, (b) H-EMRHC coated, and (c) F-EMRHC coated on CPTi.

Table 1 Surface roughness of CPTi surface and obtained surface after EMRHC process

	Before EMRHC process	After EMRHC process	
Roughness parameter	CPTi	H-EMRHC	F-EMRHC
Ra	27.7	41.8	28.9
Rq	34.5	53.0	33.4

ior of surfaces (Ref 46). It is worth mentioning that designing tissue engineering substrates with a controlled balance of hydrophilic and hydrophobic surface properties is essential for promoting cell adhesion, proliferation, and differentiation while maintaining proper biological function (Ref 47). Figure 6 shows the variation of WCA of a droplet on the CPTi and EMRHC-coated samples during 120 s. The results depicted that the water affinity of all surfaces was hydrophilic, also the WCA decreased over time for all the samples. Furthermore, the EMRHC process caused improved water affinity for biomedical applications because of increasing of the hydrophilicity. It was also found that the variation of WCA on EMRHC coatings was more stable than CPTi due to the nanotopography formed on top of the surface. The optical images of a water droplet at the beginning and end of the test on the surface of samples are presented in Fig. 6(b). Therefore, it can be predicted that the wear behavior of CPTi in a wet condition will be changed with applying the EMRHC coating.

In addition, the hardness of the top coating has a significant role in the tribology behavior of CPTi implants, because it is representative of particle bonding and adhesion to the substrate (Ref 48). Hence, the hardness of the surfaces of the samples was tested as the results given in Fig. 7(a). As a result of the H-EMRHC process, the surface hardness of the CPTi was
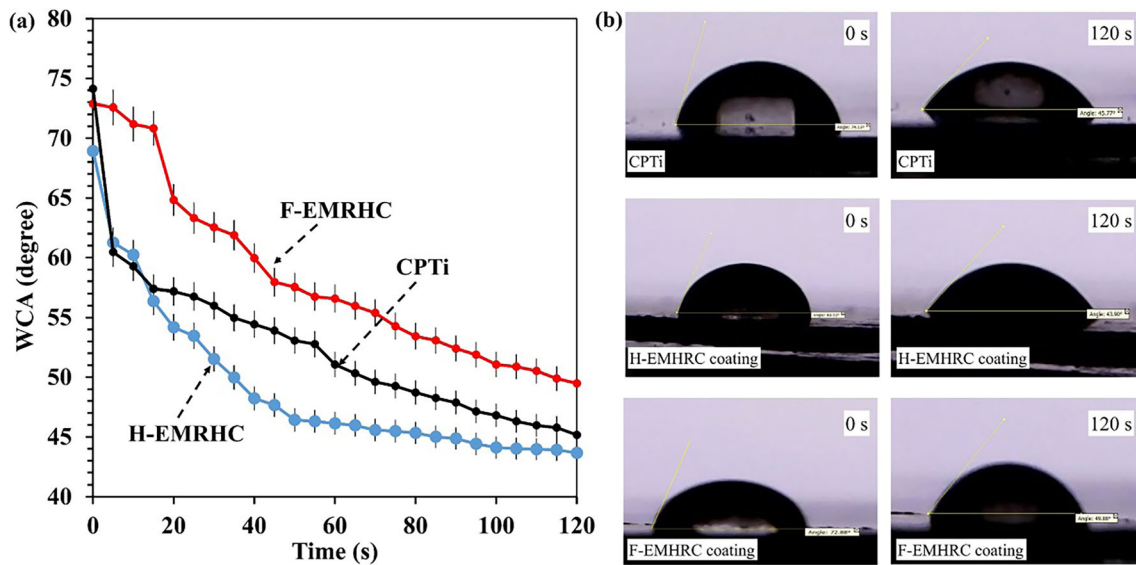
Fig. 6. Variation of WCA over 120 s (a), and (b) optical images of a water droplet on the CPTi and EMRHC-coated samples at the start and finish points of test.
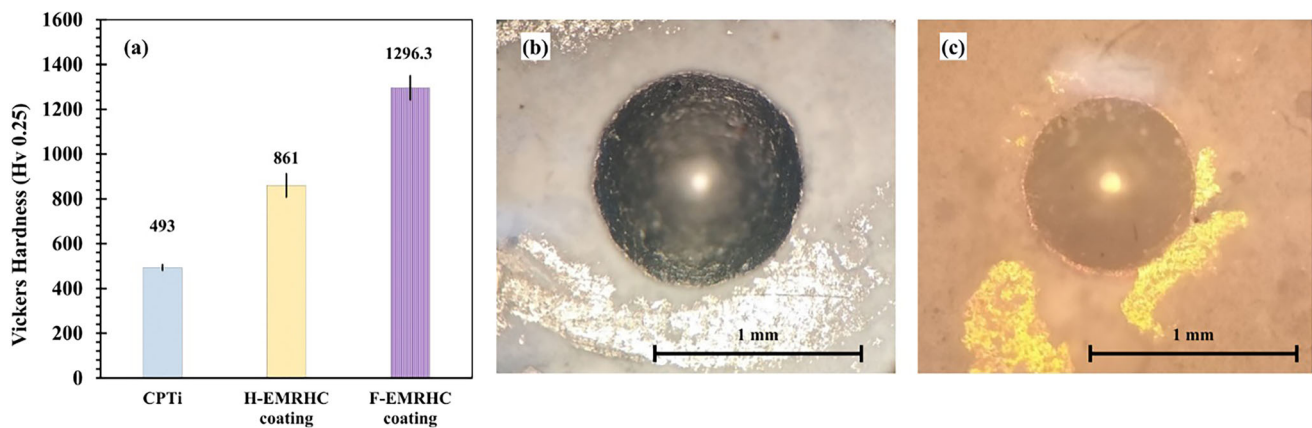

Fig. 7. The average of hardness of surface uncoated and half and full done EMRHC-coated CPTi (a). Optical image of the affected area by Rockwell-C indentation on (b) H-EMRHC and (c) F-EMRHC-coated CPTi.

increased about twice times. The F-EMRHC process increased the surface hardness value drastically compared with the H-EMRHC process. It seems to us the hybrid PVP/HA fibers could fully be melted splats and cover the surface, and products could diffuse to a longer distance from the top surface leading to the formation of strong bonds between the particles and substrate. The adhesion strength of the EMRHC coatings was examined by the Rockwell-C indentation test. According to the optical images of the indentation area, as shown in Fig. 7(b), the absence of any visible cracking or scaling in the region surrounding the indentation site was observed for both samples. Therefore, it can be said that the adhesion quality exhibited the HF1 level of the relevant standard. It suggests that the EMRHC coating is capable of withstanding significant stress and strain without compromising its structural integrity.

3.3 Residual Stress of EMRHC Coatings

The residual stress of coatings plays a significant role in wear properties (Ref 49). Since the major causes of mechanical failure are recognized by the residual stress, the residual stress generated by the EMRHC process was precisely evaluated by means of the XRD-$sin^2(\psi)$ technique. The principal equation for measuring the XRD-$sin^2(\Psi)$ is as following (Ref 31, 34, 41);

$$d_{hkl} = \left[\left(\frac{1 + v}{E} \right) sin^2(\psi) \right] \sigma d_0 + d_0 \qquad (Eq\ 6)$$

where d_{hkl} is d-spacing of (hkl) plans under stress, d_0 is the d-spacing of (hkl) plans without stress, v and E are the Poisson's ratio and Young's modulus to the (hkl) orientation of the CPTi, respectively. σ is the plane stress regarding the perpendicular two stress components. ψ is the off-axis angle with respect to the normal surface of the sample. It should be added to calculate the stress residual of EMRHC coatings, the elastic isotropy in the individual crystallites has been assumed. Also, to find the elastic isotropic plane (hkl) with respect to the individual crystallites of CPTi was selected. To do this, several x-ray scanning was performed on the normal surface at $\psi = 0$ º. The plane (103) with respect to the $2\theta = 116.025\text{-}119.975$ º was detected for the H-EMRHC coating, and plane (210) with
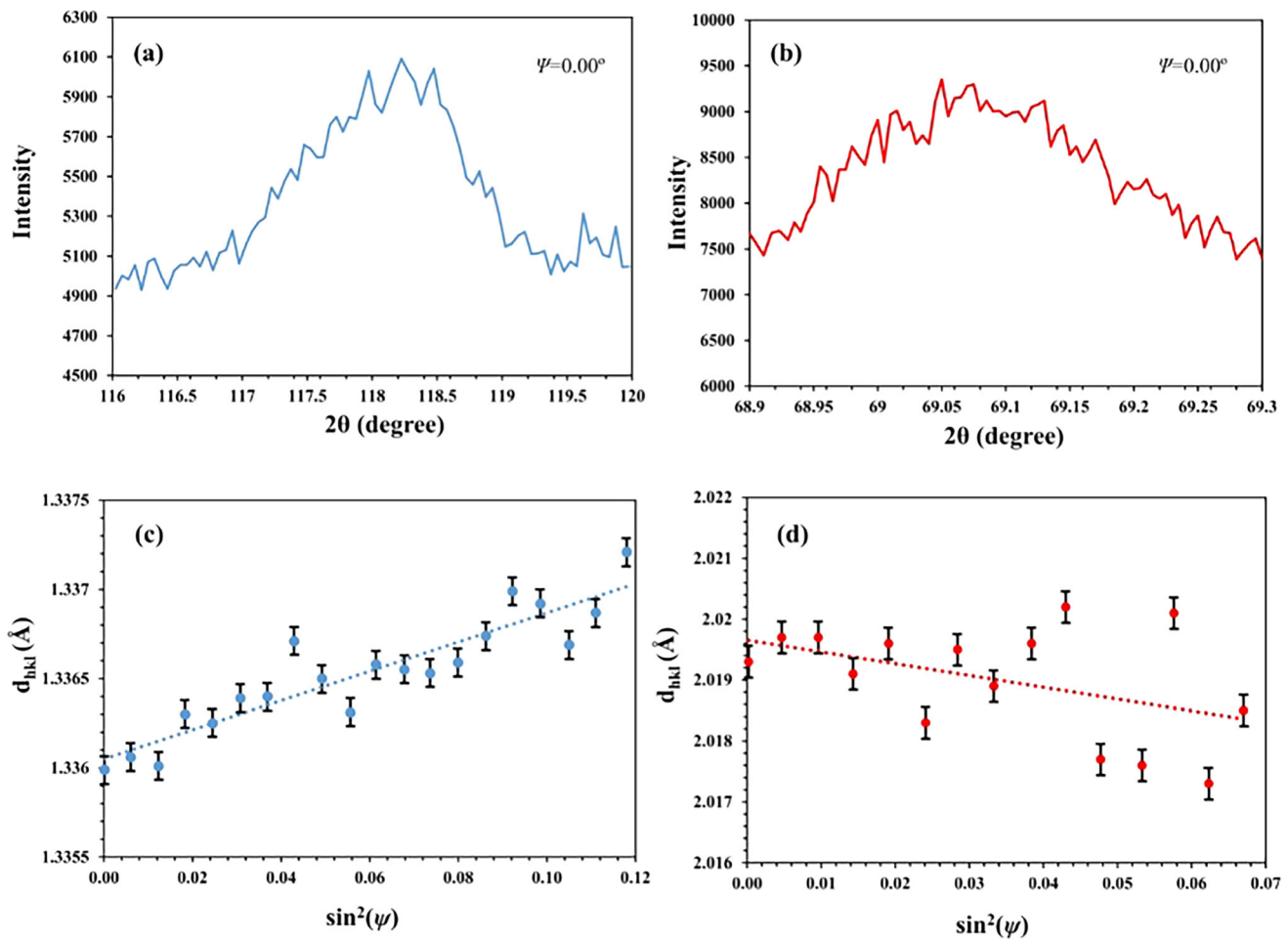
Fig. 8. The x-ray-2θ graphs ($\psi = 0$) of (a) plane (103) of H-EMRHC coating, and (b) plane (210) of F-EMRHC coating. The linear regression between d_{hkl} and $\sin^2(\psi)$ for (c) H-EMRHC and (d) F-EMRHC-coated CPTi to calculate the residual stress.

$2\theta = 68.875\text{-}69.325°$ was recognized for the F-EMRHC coating as the x-ray-2θ graphs presented in Fig. 8(a) and (b). It is worth mentioning that the calculation of the 2θ position is not a simple process and often it has systematic errors, especially for a broad and asymmetric peak that has been diffracted at a high 2θ position. To achieve the precise d-spacing, the Lorentz–Polarization factor was applied to the $I\text{-}2\theta$ data (Ref 41, 50, 51). Hence, the error bars were considered via calculating the d_{hkl} and $\sin^2(\psi)$ for a known 2θ. The σ can be achieved by the linear regression analyzing the d_{hkl} -$\sin^2(\psi)$. The linear fitting on d_{hkl} -$\sin^2(\psi)$ data for H- and F-EMRHC coatings is presented in Fig. 8(c) and (d). The results showed that the residual stress was 591 ± 89 and -189 ± 42 MPa with respect to the H- and F-EMRHC coatings. The origin of residual stress can be considered to the heating flow during the EMRHC process. The tensile residual stress on the CPTi after H-EMRHC processing is due to the inhomogeneous heating and cooling of the surface. Our findings reveal that the inner Ti metal received the further ceramic aggregate, the coating could be cooled more slowly than H-EMRHC processing, and subsequently the compressive stress was generated alongside the F-EMRHC-coated CPTi (Ref 33). Our findings are in good agreement with others. Singh et al. (Ref 52) also found that the post heat treatment of coating is a helpful method to decrease the residual stresses of HA coatings on titanium alloy-based implants.

Moreover, the thickness of the coating has a significant role in residual stress implied in the coating–substrate (Ref 53). Although a non-homogeneous heating flow was carried out during F-EMRHC processing, the longer the diffusion pathway, and the higher interactions between the preliminary HA source and Ti caused to create the thicker products on the Ti substrate. However, the stress concentration was decreased due to the higher thickness, and therefore, it hindrances the microcracks and delamination through in the F-EMRHC coating. Our findings are in good agreement with others. Vereschaka et al. (Ref 54) studied the residual stress issued by the variety of thicknesses of nanolayer composite coatings. They also found that the tensile stress was observed when the thickness was 2-5.9 μm, while it was transferred to compressive stress when the thickness was 8.5 μm. In addition to the thickness, the hardness of the coatings is another variable that influences the residual stress of the coating. The mechanism is a bit complicated. The coating with a higher hardness has a higher elastic modulus and probably an interface with a higher coherency exists on the substrate; therefore, a higher residual stress (compressive stress) is formed (Ref 55). As explained, the hard products of the F-EMRHC process (e.g., Ti_5P_3, $CaTiO_3$, CaO, and TiO_2) could diffuse to a longer distance from the top surface leading to the formation of strong bonds between the particles and substrate. Our findings are in good agreement with others. For example, Bielawski et al. (Ref 56) recognized that the higher

residual stress is observed by the coatings with the higher hardness values. Finally, it can be added that the roughness of the coating also affects the calculations. The higher roughness strongly influences the measured residual stress (Ref 57). According to the roughness values given in Table 1, the lower error of residual stress was obtained for F-EMRHC coating (15.0 %) in compassion with H-EMRHC (22.2 %) coating due to the lower roughness values.

3.4 Effect of Residual stress on Tensile strength

The mechanical properties of titanium-based implants have a severe impact on biomedical applications (Ref 58). Valuable data can be obtained from the strain–stress curve to recognize the role of EMRHC coatings. Figure 9 illustrates the tensile behavior of CPTi and EMRHC-coated CPTi samples. The yield strength, Young's module, ultimate compressive strength (UTS), and toughness were calculated, and the results are given in Table 2. A significant increase in yield strength, Young's module, and UTS was observed for both EMRHC-coated samples. In contrast, the toughness decreased because of the brittle nature of the coatings, and lost some of their ability to plastic deformation before the failure. The improvement of mechanical properties can be explained by the roles of the CPTi substrate and CaP coating created on the CPTi via the EMRHC process. The heat treatment during EMRHC for modification of the mechanical properties of CPTi grade 2 cannot be considered due to the single-phase α structure of CPTi; in addition, the grain growth cannot be occurred because of the very fast heat treatment (Ref 59). Therefore, it can be elucidated that the mechanical improvement by the EMRHC process is not due to the role of the titanium substrate. In contrast, the rapid heating and cooling via the EMRHC process, and also the formation of CaP coating were responsible for remaining the stress and hard ceramic coating on the CPTi. According to the results, the highest mechanical properties can be considered for the F-EMRHC coating. Since the thickness of the samples for the tensile test and residual test by the XRD method was almost the same, therefore there is a meaningful comparison between mechanical behavior and residual stress explained above. The compressive residual stress, thicker interaction zone, and higher hardness are the main reasons for these achievements for F-EMRHC coating.

3.5 Effect of Residual Stress on Wear Studies

The analysis of the frictional response curves allows for the identification of distinct periods or regimes of friction and wear properties. The variation of the coefficient of friction (COF) by sliding over 100 m in the dry and SBF environments is plotted in Fig. 10. The results indicated that the COF was changed at several steps in the dry condition. At the first step of sliding, the COF of CPTi was increased rapidly due to its ductile surface (Ref 60), while the H-EMRHC-coated sample presented the opposite behavior, and the F-EMRHC-coated sample displayed almost the stable behavior. This is because the EMRHC coating could provide a hard shield against the attack on the surface. A slight decrease in the COF of H-EMRHC-coated samples was possibly due to the third part formed on the worn track of the sample which may act as a solid lubricant (Ref 60). The compressive residual stress on the F-EMRHC-coated samples prevented the ceramic phases such as α-TCP, CaO, TiO$_2$, CTO, and Ti$_5$P$_3$ to release between the sliding surfaces. Swathing to the next step occurred by a significant increase in the COF of
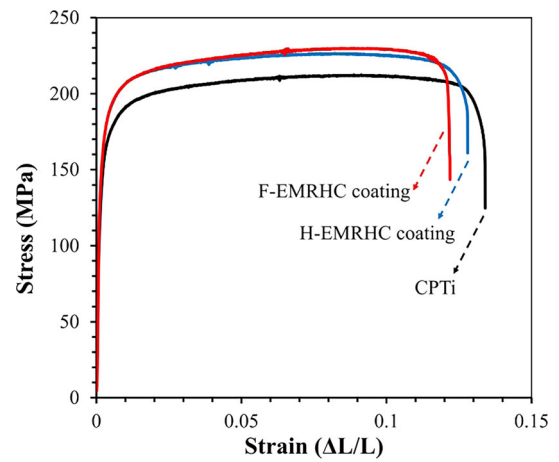

Fig. 9. Stress–strain curve of CPTi and EMRHC-coated samples.

Table 2 Mechanical properties of CPTi and EMRHC-coated samples

Sample code	Yield strength	UTS	Young module	Toughness
	MPa	MPa	GPa	MPa
CPTi	181.8	212.4	103.3	27.2
H-EMRHC	202.8	226.4	108.2	27.8
F-EMRHC	204.1	229.7	112.3	26.8

all samples which was caused by fragmentation and degradation of the third body, leading to an abrasive role (Ref 61). Although the EMRHC process caused to jump of the COF at a less distance of wear, the more stable COF was detected for the EMRHC-coated samples. Furthermore, our findings confirmed that the crystalline and hard phases with high integrity of coating with Ti substrate can be obtained easily by the EMRHC process. It is worth mentioning that the EMRHC-coated samples depicted a lower COF compared to the CPTi when those were worn in the SBF solution (Fig. 10b). All samples presented almost a steady state in friction coefficient changes during the continuous contact between the pin and sample surface in the SBF solution. The average COF of the EMRHC-coated samples was 0.144 and 0.163 with respect to the H- and F-EMRHC coatings. The easier formation of the hydroxyl bonds with the ceramic phases at the top more hydrophilic surface of the EMRHC coatings, namely by α-TCP and CTO, on one hand, and precipitation of bone-like apatite on the bioactive surface of EMRHC coatings on another hand (Ref 29) could act as the solid lubricants. It should be added that a wear test in the SBF solution plays the real conditions for an implant (Ref 54), so our results strongly suggest the EMRHC process to improve the wear resistance of the CPTi implants.

To understand the wear mechanism and rate, the worn area was studied by SEM images, and the weight loss was measured over 100 m by sliding the steel pin on the samples. Figure 11 presents the micrographs of worn surfaces in the dry and in the SBF solution. Upon analysis of the surfaces, it was exhibited that the CPTi had a ductility manner in both dry and wet conditions, which is indicative of a certain level of the shape forming (Ref 62). Also, a more uniform microstructure was
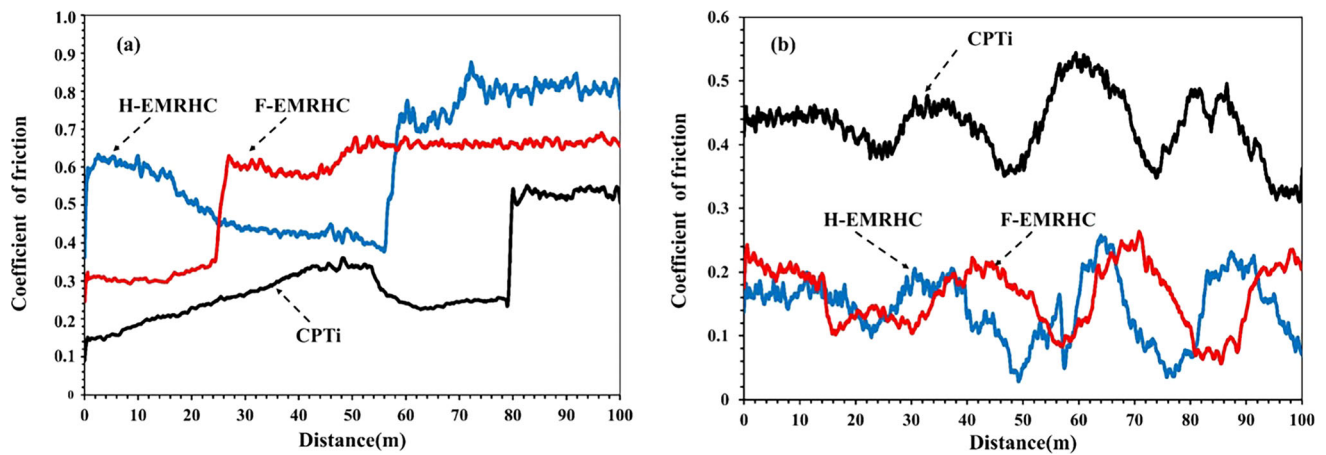
Fig. 10. Variation of coefficient of friction of the CPTi and EMRHC coatings in (a) dry and (b) in SBF solution conditions.
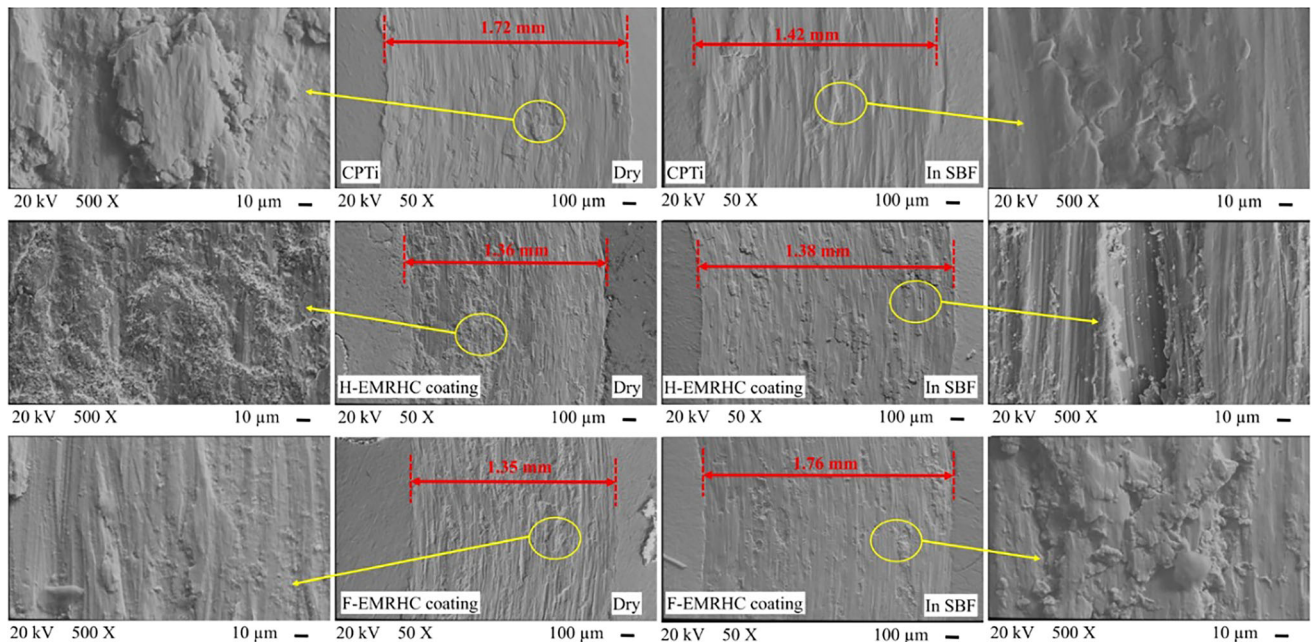

Fig. 11. SEM micrographs of the worn track of the samples in dry and in the SBF solution. The higher magnifications from the marked areas have been presented on the left and right sides.

observed for the CPTi surfaces. It seems to us that the scratch-like abrasion and adhesive were the main dominant wear mechanism on the CPTi and EMRHC-coated samples in the dry condition, respectively. In addition, the abrasion pattern observed in the dry environment for the pure titanium sample exhibits a bimodal distribution, whereas, in the EMRHC-coated samples, the distribution was trimodal (Ref 60). It should be noted that the mentioned mechanisms were almost observed for the samples, but the adhesive abrasion on the EMRHC-coated samples was performed a little more gently. It is because of the ability of the EMRHC coatings to form the bone-like apatite (Ref 29). The precipitations of bone-like apatite could act as solid lubricants, and subsequently, a soft-adhesive surface was observed.

Further investigation was also performed on the cross-sectional area of the worn tracks. The cross-sectional area of worn tracks in dry and in SBF conditions is presented in Fig. 12. The results indicated that the depth of track for all

samples was intensified via wearing in the SBF environment. The weight loss and specifications of the worn track are presented in Table 3. According to the depth of the track, it was confirmed that not only the coating but also the titanium substrate was worn. However, the results showed that the wear resistance of CPTi was enhanced by applying the EMRHC coatings in the dry condition which is attributed to the hard top protective coatings. Also, it was noted that the mechanical properties of CPTi were enhanced by applying the EMRHC coatings. Therefore, after stabilizing the COF, the lower wear rate could be evaluated for the EMRHC coatings. However, complex behavior can be explained for the samples worn in the SBF solution. The weight loss of the CPTi in the SBF solution was the same in dry conditions, and the volume of worn tracks in H- and F-EMRHC coatings was almost the same in SBF conditions while the weight loss was different. This is because of the bio-inert nature of titanium and its alloys (Ref 63). In contrast, the bioactive EMRHC coatings caused the formation
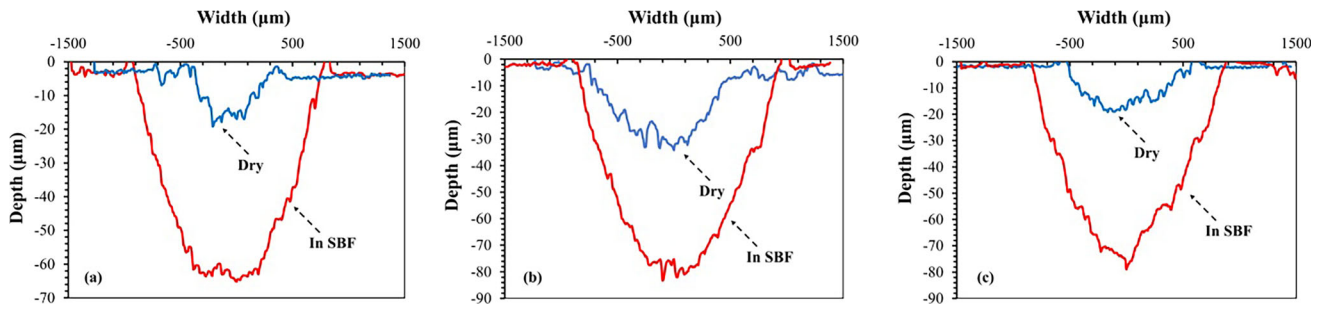
Fig. 12. Cross view profilometer of wear track of (a) CPTi, (b) H-EMRHC coated, and (c) F-EMRHC coated on CPTi in the dry and in the SBF solution tests.

Table 3 Coefficient of friction, weight loss, and geometry of worn track

Sample code	Wear environment	COF ...	Weight loss, mg	Wear width*, mm	Wear depth*, μm	Track volume, mm^3
CPTi	dry	0.3036	0.0078	1.63	19.17	0.015
	in SBF	0.4306	0.0078	1.78	65.18	0.058
H-EMRHC	dry	0.6075	0.0025	1.27	34.3	0.022
	in SBF	0.1444	0.0098	1.68	82.2	0.069
F-EMRHC	dry	0.5503	0.0025	1.08	18.2	0.010
	in SBF	0.1635	0.0071	1.78	78.8	0.070

*Average of measurements

of bone-like apatite during the wear test in the SBF solution, and therefore in addition to the worn debris, the extra bone-like apatite precipitations were measured. As explained above, the higher bioactivity of F-EMRHC coating caused to precipitate of further bone-like apatite, and therefore, they acted like solid lubricants, and subsequently, a lower wear rate was observed. In addition to the above, the compressive residual stress on the F-EMRHC coating could arm the CPTi surface against the force attack, and therefore, it enhanced the wear resistance.

To explore the nature of the debris, the microstructures of the debris were investigated as FESEM images shown in Fig. 13. The results exhibited the spherical particles for the debris released from the CPTi, and polygonal particles for EMRHC coatings worn in dry conditions. The polygonal particles may be originated from α-TCP, CaO, TiO$_2$, CTO, and Ti$_5$P$_3$ components. In contrast, the clusters with a cauliflower-like shape which is the nature of the apatite were also observed beside the released particles (Ref 64). To ensure, the EDS analysis was carried out to identify the chemical composition of debris. The EDS spectra provided from the debris are presented in Fig. 14. It was found that the titanium was the nature of debris released from the CPTi in both conditions. The results confirmed the presence of Ti, Ca, and P in debris released from the EMRHC coatings attributing to the α-TCP, CaO, TiO$_2$, CTO, and Ti$_5$P$_3$ components. Also, intensifying of Ca and P elements in spectra of released debris from SBF solution demonstrates the formation of bone-like apatite.

4. Conclusions

The CPTi surface was modified by the EMRHC process. The results indicated that the preliminary HA reacted with the CPTi substrate, and therefore, α-TCP, CaO, TiO$_2$, CTO, and Ti$_5$P$_3$ were obtained over the EMRHC process. The roughness of CPTi substrate increased by applying the EMRHC coatings. It was found that the nanotopography was formed on the F-EMRHC coating. The hardness of CPTi was 493 Hv, while it was increased about two and three times with H- and F-EMRHC process. All mechanical characteristics were enhanced by applying the EMRHC process. Our studies revealed that the tensile $+ 591 \pm 89$ and compressive $- 189 \pm 42$ MPa residual stress remained on the surface over half and full done EMRHC process, respectively. The COF of EMRHC coatings in the dry conditions was raised at a lower sliding distance compared to CPTi, while almost stable friction was observed. In contrast, the COF value decreased significantly in the SBF test. The weight loss in the dry conditions from the EMRHC coatings was lower than CPTi; H-EMRHC coating presented a higher value when it was exposed to the SBF solution. The SBF created a harsher environment due to the precipitation of the bone-like apatite particles on the EMRHC coatings. The debris analysis revealed that bone-like apatite was also released in addition to the main components of the EMRHC coatings. Eventually, it can be concluded that the full done MRHC
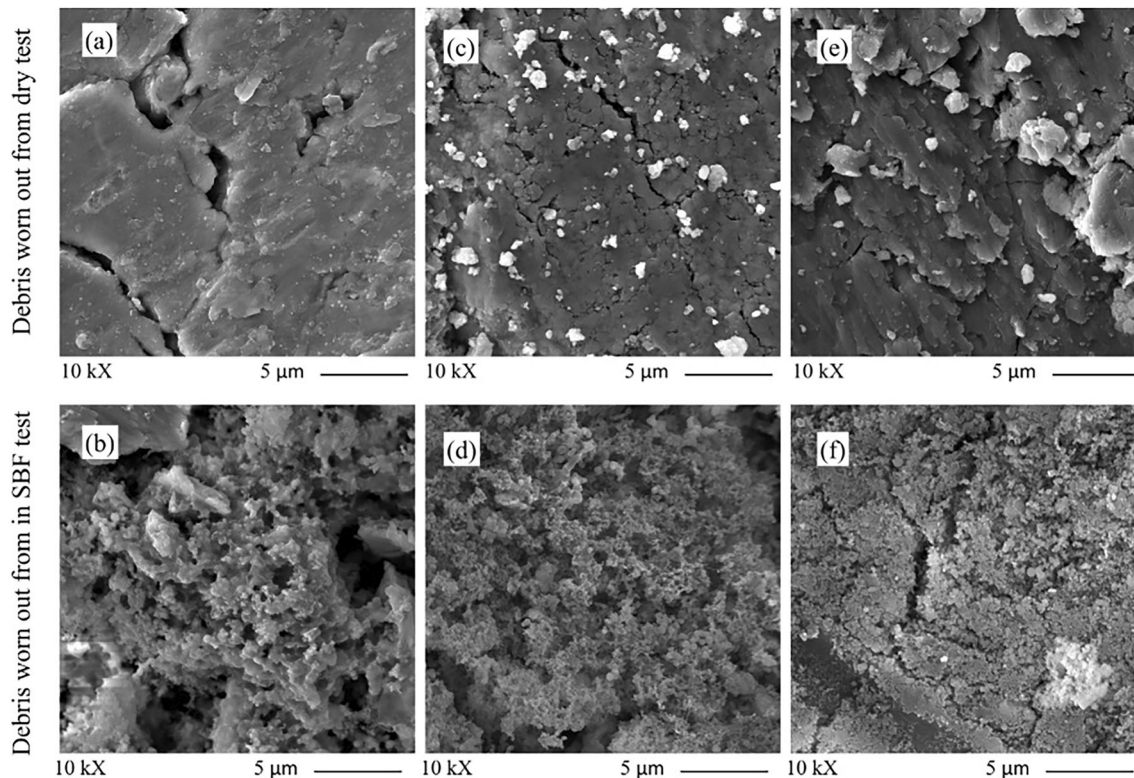
Fig. 13. FESEM images of debris released from the (a, b) CPTi, (c, d) H-EMRHC-coated, and (e, f) F-EMRHC-coated samples tested in the dry and in the SBF solution tests.
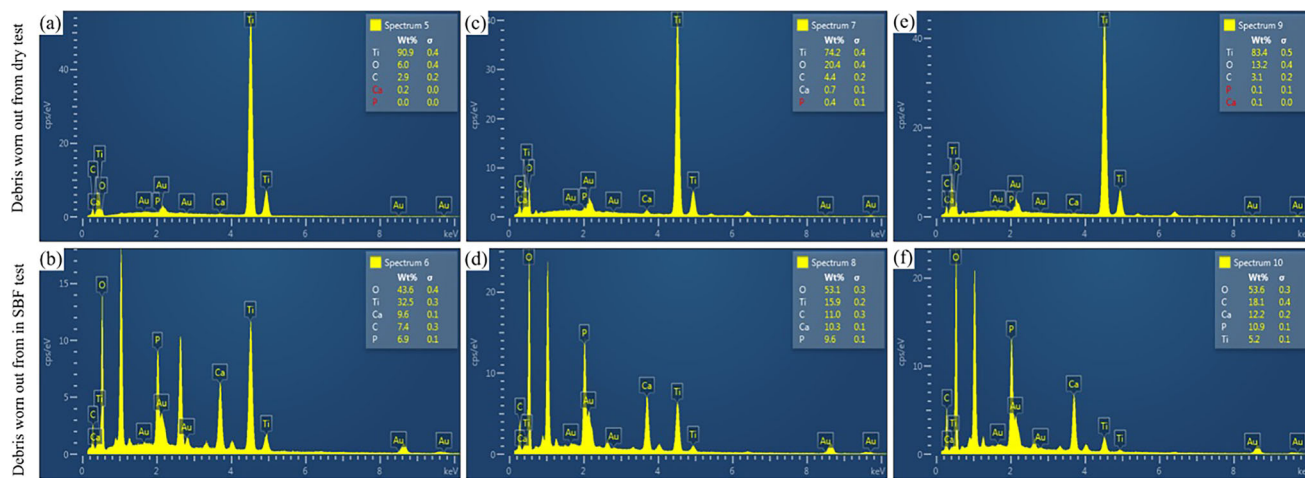

Fig. 14. EDS spectra of debris released from the (a, b) CPTi, (c, d) H-EMRHC-coated, and (e, f) F-EMRHC-coated samples tested in the dry and in the SBF solution tests.

coating had the highest wear resistance and compressive residual stress which can be strongly suggested for modification of titanium-based implants.

Author Contributions

KSH was involved in writing—original draft preparation, formal analysis, and investigation. MY took part in writing—original draft preparation, formal analysis, and investigation. HE contributed to conceptualization, writing—original draft preparation, validation, writing—review and editing, and supervision.

Data availability

The raw/processed data required to reproduce these findings cannot be shared at this time as the data also forms part of an ongoing study.

References

1. Z. Jing, Q. Cao, and H. Jun, Corrosion, Wear and Biocompatibility of Hydroxyapatite Bio-functionally Graded Coating on Titanium Alloy Surface Prepared by Laser Cladding, *Ceram. Int.*, 2021, **47**, p 24641–24651. https://doi.org/10.1016/j.ceramint.2021.05.186

2. P.K. Rai, D. Naidu, S.K. Vajpai, B. Sharma, K. Ameyama, and K. Mondal, Effect of Cold Rolling and Heat Treatment on Corrosion and Wear Behavior of β-Titanium Ti-25Nb-25Zr Alloy, *J. Mater. Eng. Perform.*, 2021, **30**, p 4174–4182. https://doi.org/10.1007/s11665-021-05739-8

3. Y. Zhang, S. Luo, Q. Wang, and C. Seshadri Ramachandran, Effect of Hydrothermal Treatment on the Surface Characteristics and Bioactivity of HAP based MAO Coating on Ti-6Al-4V Alloy, *Surf. Coat. Technol.*, 2023, **464**, p 129566. https://doi.org/10.1016/j.surfcoat.2023.129566

4. S. Hussain, Z.A. Shah, K. Sabiruddin, and A.K. Keshri, Characterization and Tribological Behaviour of Indian Clam Seashell-derived Hydroxyapatite Coating Applied on Titanium Alloy by Plasma Spray Technique, *J. Mech. Behave. Biomed. Mater.*, 2023, **137**, p 105550. https://doi.org/10.1016/j.jmbbm.2022.105550

5. Z.Y. Zhang, T.Y. Huang, D.J. Zhai, H.B. Wang, K.Q. Feng, and L. Xiang, Study on Strontium Doped Bioactive Coatings on Titanium Alloys Surfaces by Micro-arc Oxidation, *Surf. Coat. Technol.*, 2022, **451**, p 129045. https://doi.org/10.1016/j.surfcoat.2022.129045

6. M. Madhusmita and N. Arunachalam, Effects of Electrophoretic Deposited Graphene Coating Thickness on the Corrosion and Wear Behaviors of Commercially Pure Titanium, *Surf. Coat. Technol.*, 2022, **450**, p 128946. https://doi.org/10.1016/j.surfcoat.2022.128946

7. Y. Wu, A.H. Wang, Z. Zhang, H.B. Xia, and Y.N. Wang, Wear Resistance of in Situ Synthesized Titanium Compound Coatings Produced by Laser Alloying Technique, *Surf. Coat. Technol.*, 2014, **258**, p 711–715. https://doi.org/10.1016/j.surfcoat.2014.08.012

8. M. Kheradmandfard, O.V. Penkov, S.F. Kashani-Bozorg, J.S. Lee, C.L. Kim, M. Khadem, S.W. Cho, A.Z. Hanzaki, and D.E. Kim, Exceptional Improvement in The Wear Resistance of Biomedical β-type Titanium Alloy with the use of a Biocompatible Multilayer Si/DLC Nanocomposite Coating, *Ceram. Int.*, 2022, **48**, p 17376–17384. https://doi.org/10.1016/j.ceramint.2022.03.002

9. T. Sun, N. Xue, C. Liu, C. Wang, and J. He, Bioactive (Si, O, N)/(Ti, O, N)/Ti Composite Coating on NiTi Shape Memory Alloy for Enhanced Wear and Corrosion Performance, *Appl. Surf. Sci.*, 2015, **356**, p 599–609. https://doi.org/10.1016/j.apsusc.2015.07.185

10. R.C. Costa, J.G.S. Souza, J.M. Cordeiro, M. Bertolini, E.D. de Avila, R. Landers, E.C. Rangel, C.A. Fortulan, B. Retamal-Valdes, N.C. da Cruz, M. Feres, and V.A.R. Barão, Synthesis of Bioactive Glass-based Coating by Plasma Electrolytic Oxidation: Untangling a New Deposition Pathway Toward Titanium Implant Surfaces, *J. Colloid Interface Sci.*, 2020, **579**, p 680–698. https://doi.org/10.1016/j.jcis.2020.06.102

11. D. Kuczyńska-Zemła, J. Pura, B. Przybyszewski, M. Pisarek, and H. Garbacz, A Comparative Study of Apatite Growth and Adhesion on a Laser-Functionalized Titanium Surface, *Tribol. Int.*, 2023, **182**, p 108338. https://doi.org/10.1016/j.triboint.2023.108338

12. A. Błoniarz, K. Cholewa-Kowalska, M. Gajewska, B. Grysakowski, and T. Moskalewicz, Electrophoretic Deposition, Microstructure and Selected Properties of Nanocrystalline SnO2/Sr Enriched Bioactive Glass/Chitosan Composite Coatings Titanium, *Surf. Coat. Technol.*, 2020, **450**, p 129004. https://doi.org/10.1016/j.surfcoat.2022.129004

13. H. Shaygani, S. Seifi, A. Shamloo, M. Golizadeh, S.Y. Rahnamaee, M. Alishiri, and S. Ebrahimi, Novel Bilayer Coating on Gentamicin-loaded Titanium Nanotube for Orthopedic Implants Applications, *Int. J. Pharm.*, 2023, **636**, p 122764. https://doi.org/10.1016/j.ijpharm.2023.122764

14. C. Skjoldebrand, J.L. Tipper, P. Hatto, M. Bryant, and R.M. Hall, Cecilia Persson Current Status and Future Potential of Wear-resistant Coatings and Articulating Surfaces for Hip and Knee Implants, *Mater. Today Bio.*, 2020, **15**, p 100270. https://doi.org/10.1016/j.mtbio.2022.100270

15. Y. Fang, Simulation and Experiment of Impact Effects of Nanosecond Pulse Laser-Generated Processing Ti-6Al-4V Alloy, *J. Mater. Eng. Perform.*, 2021, **30**, p 5515–5523. https://doi.org/10.1007/s11665-021-05551-4

16. A. Ghailane, E.Y. Maadane, A. Barchid, S. Berchane, S. Badre-Eddine, H. Larhlimi, C.B. Fischer, J. Alami, and M. Makha, Influence of Annealing Temperature on the Microstructure and Hardness of TiN Coatings Deposited by High-Power Impulse Magnetron Sputtering, *J. Mater. Eng. Perform.*, 2022, **31**, p 5593–5601. https://doi.org/10.1007/s11665-022-06689-5

17. E.Z. Nahum, S. Lugovskoy, A. Lugovskoy, B. Kazanski, and A. Sobolev, The Study of Hydroxyapatite Growth Kinetics on CP e Ti and Ti65Zr Treated by Plasma Electrolytic Oxidation Process, *J. Market.*

Res., 2023, **24**, p 2169–2186. https://doi.org/10.1016/j.jmrt.2023.03.128

18. O.V. Tkachuk, I.M. Pohrelyuk, R.V. Proskurnyak, J. Morgiel, M. Faryna, and A. Goral, Morphology and Corrosion Resistance of Hydroxyapatite Coatings Formed on Commercially Pure Titanium, *J. Mater. Eng. Perform.*, 2023 https://doi.org/10.1007/s11665-023-07910-9

19. M. Samiksha, R. Gnanamoorthy, and Y. Otsuka, Fretting Wear Characteristics of Suspension Plasma-Sprayed Hydroxyapatite Coating on Titanium Substrate for Orthopedic Applications, *J. Mater. Eng. Perform.*, 2022, **31**, p 7290–7301. https://doi.org/10.1007/s11665-022-06753-0

20. A. Alcantara-Garcia, A. Garcia-Casas, and A. Jimenez-Morales, Electrochemical study of the synergic effect of phosphorus and cerium additions on a sol-gel coating for Titanium manufactured by powder metallurgy, *Prog. Org. Coat.*, 2018, **124**, p 267–274. https://doi.org/10.1016/j.porgcoat.2018.01.026

21. U. Rokkala, G. Suresh, and M.R. Ramesh, Comparative Study of Plasma Spray and Friction Stir Processing on Wear Properties of Mg-Zn-Dy Alloy, *J. Mater. Eng. Perform.*, 2023 https://doi.org/10.1007/s11665-023-08087-x

22. M. Yadi, H. Esfahani, M. Sheikhi, and M. Mohammadi, CaTiO3/α-TCP Coatings on CP-Ti Prepared via Electrospinning and Pulsed Laser Treatment for in-vitro Bone Tissue Engineering, *Surf. Coat. Technol.*, 2020, **401**, p 126256. https://doi.org/10.1016/j.surfcoat.2020.126256

23. R. Gorejov, P. Oriňaková, Z.O. Králová, T. Sopčák, I. Šišoláková, M. Schnitzer, M. Kohan, and R. Hudák, Electrochemical Deposition of a Hydroxyapatite Layer onto the Surface of Porous Additively Manufactured Ti6Al4V Scaffolds, *Surf. Coat. Technol.*, 2023, **455**(25), p 129207. https://doi.org/10.1016/j.surfcoat.2022.129207

24. H. Esfahani, R. Jose, and S. Ramakrishna, Electrospun Ceramic Nanofiber Mats Today: Synthesis, Properties, and Applications, *Materials*, 2017, **10**(11), p 1238. https://doi.org/10.3390/ma10111238

25. H. Esfahani, E. Salahi, A. Tayebifard, M.R. Rahimipour, and M. Keyanpour-Rad, Influence of Zinc Incorporation on Microstructure of Hydroxyapatite to Characterize the Effect of pH and Calcination Temperatures, *J. Asian Ceramic Soc.*, 2014, **2**, p 248–252. https://doi.org/10.1016/j.jascer.2014.05.001

26. H. Esfahani, M. Darvishghanbar, and B. Farshid, Enhanced Bone Regeneration of Zirconia-toughened Alumina Nanocomposites Using PA6/HA Nanofiber Coating via Electrospinning, *J. Mater. Res.*, 2018, **33**(24), p 4287–4295. https://doi.org/10.1557/jmr.2018.391

27. V. Rattan, T.S. Sidhu, and M. Mittal, Wear Studies on Plasma-Sprayed Pure and Reinforced Hydroxyapatite Coatings, *Mater. Today Proc.*, 2022, **60**, p 1731–1735. https://doi.org/10.1016/j.matpr.2021.12.306

28. F. Musharavati, F. Jaber, M. Nasor, M. Sarraf, E.Z. Nezhad, K. Uzun, Y. Ma, S. Bae, R. Singh, and M.E. Chowdhury, Micromechanical Properties of Hydroxyapatite Nanocomposites Reinforced with CNTs and ZrO2, *Ceram. Int.*, 2023, **49**(5), p 7466–7475. https://doi.org/10.1016/j.ceramint.2022.10.218

29. M. Yadi, H. Esfahani, A. Nourian, S.H. Navard, and A. Fattahalhosseini, Surface Modification of CP-Ti by Calcium-Phosphate via an Integrated Electrospinning and Rapid Heating and Cooling (EMRHC) process: Essential in-vitro Studies for Bone Regeneration, *Surf. Int.*, 2021, **27**, p 101480. https://doi.org/10.1016/j.surfin.2021.101480

30. V. Baranauskas, H.J. Ceragioli, A.C. Peterlevitz, and M. Fontana, Low Residual Stress Diamond Coatings on Titanium, *Surf. Coat. Technol.*, 2005, **200**, p 2343–2347. https://doi.org/10.1016/j.surfcoat.2005.04.020

31. Y.C. Yang, E. Chang, B.H. Hwang, and S.Y. Lee, Biaxial Residual Stress States of Plasma-sprayed Hydroxyapatite Coatings on Titanium Alloy Substrate, *Biomaterials*, 2000, **21**, p 1327–1337.

32. C.L. Chang, J.I. Jao, W.Y. Ho, and D.Y. Wang, Effects of Titanium-Implanted Pre-Treatments on the Residual Stress of TiN Coatings on High-speed Steel Substrates, *Surf. Coat. Technol.*, 2007, **201**, p 6702–6706. https://doi.org/10.1016/j.surfcoat.2006.09.035

33. A.R. Nimkerdphol, Y. Otsuka, and Y. Mutoh, Effect of Dissolution/precipitation on the Residual Stress Redistribution of Plasma-sprayed Hydroxyapatite Coating on Titanium Substrate in Simulated Body Fluid (SBF), *J. Mech. Behav. Biomed. Mater.*, 2014, **36**, p 98–108. https://doi.org/10.1016/j.jmbbm.2014.04.007

34. Y.C. Yang and E. Chang, Measurements of Residual Stresses in Plasma-sprayed Hydroxyapatite Coatings on Titanium Alloy, *Surf. Coat. Technol.*, 2005, **190**, p 122–131. https://doi.org/10.1016/j.surfcoat.2004.02.038

35. C.H. Huang and M. Yoshimura, Biocompatible Hydroxyapatite Ceramic Coating on Titanium Alloys by Electrochemical Methods via Growing Integration Layers [GIL] Strategy: A Review, *Ceramics Int.*, 2023 https://doi.org/10.1016/j.ceramint.2022.12.248

36. A. Umapathi and S. Swaroop, Measurement of Residual Stresses in Titanium Alloys using Synchrotron Radiation, *Measurement*, 2019, **140**, p 518–525. https://doi.org/10.1016/j.measurement.2019.04.021

37. V. Koshuro, E. Osipova, O. Markelova, M. Fomina, A. Zakharevich, S. Pichkhidze, and A. Fomin, Titanium Oxide Coatings Formed by Plasma Spraying Followed by Induction Heat Treatment, *Ceramics Int.*, 2023, **49**, p 2034–2043. https://doi.org/10.1016/j.ceramint.2022.09.169

38. S. Park, J. Choi, S. Mondal, T.M.T. Vo, V.H. Pham, H. Lee, S.Y. Nam, C.-S. Kim, and O. Junghwan, The Impact of Cu(II) Ions Doping in Nanostructured Hydroxyapatite Powder: A Finite Element Modelling Study for Physico-mechanical and Biological Property Evaluation, *Adv. Powder Technol.*, 2022, **33**(2), p 103405. https://doi.org/10.1016/j.apt.2021.103405

39. A. Ebrahimi, H. Esfahani, A. Fattah-alhosseini, and O. Imantalab, Electrochemical Properties of Commercially Pure Ti with TiB/TiB₂ Coatings in Hanks Balanced Salt Solution, *J. Mater. Eng. Perform.*, 2019, **28**, p 1456–1468. https://doi.org/10.1007/s11665-019-03930-6

40. T. Kokubo and H. Takadama, How useful is SBF in Predicting in vivo Bone Bioactivity?, *Biomaterials*, 2006, **27**(15), p 2907–2915. https://doi.org/10.1016/j.biomaterials.2006.01.017

41. Cullity, Bernard Dennis. Elements of x-ray Diffraction. Addison-Wesley Publishing, (1956) Chapter 17

42. S. Panda, B. Prasad Behera, S. Kumar Bhutia, C. Kumar Biswas, and S. Paul, Rare Transition Metal Doped Hydroxyapatite Coating Prepared via Microwave Irradiation Improved Corrosion Resistance, Biocompatibility and Anti-biofilm Property of Titanium Alloy, *J. Alloys Compd.*, 2022, **918**, p 165662. https://doi.org/10.1016/j.jallcom.2022.165662

43. H. Shi, X. Wu, S. Sun, C. Wang, Z. Vangelatos, A. Ash-Shakoor, C.P. Grigoropoulos, P.T. Mather, J.H. Henderson, and Z. Ma, Profiling the Responsiveness of Focal Adhesions of Human Cardiomyocytes to Extracellular Dynamic Nano-topography, *Bioactive Mater.*, 2022, **10**, p 367–377. https://doi.org/10.1016/j.bioactmat.2021.08.028

44. Q. Zan, C. Wang, L. Dong, P. Cheng, and J. Tian, Effect of Surface Roughness of Chitosan-based Microspheres on Cell Adhesion, *Appl. Surf. Sci.*, 2008, **255**(2), p 401–403. https://doi.org/10.1016/j.apsusc.2008.06.074

45. S. Balcı and F. Tomu, Catalytic Wet Peroxide Oxidation of Phenol Through Mesoporous Silica-pillared Clays Supported Iron and/or Titanium Incorporated Catalysts, *J. Environ. Manag.*, 2023, **326**(Part B), p 116835. https://doi.org/10.1016/j.jenvman.2022.116835

46. J.C. Sánchez-López, M. Rodríguez-Albelo, M. Sánchez-Pérez, V. Godinho, C. López-Santos, and Y. Torres, Ti6Al4V Coatings on Titanium Samples by Sputtering Techniques: Microstructural and Mechanical Characterization, *J. Alloy. Compd.*, 2023, **953**, p 170018. https://doi.org/10.1016/j.jallcom.2023.170018

47. W.O.S. Seeram Ramakrishna, M. Ramalingam, and T.S. Sampath Kumar, *Biomaterials A Nano Approach*, 1st ed. CRC Press, Florida, 2010

48. S. Kumar and A. Kumar Das, Wear Resistance and Hardness Properties of TiB2– Fe Coating Developed on AISI 1020 Steel by Tungsten Inert Gas (TIG) Cladding, *Ceramint. Int.*, 2022, **48**(20), p 30052–30065. https://doi.org/10.1016/j.ceramint.2022.06.274

49. S.P. Chodisetti and B.V.M. Kumar, Tailoring Friction and Wear Properties of Titanium Boride Reinforced Silicon Carbide Composites, *Wear*, 2023, **526–527**, p 204886. https://doi.org/10.1016/j.wear.2023.204886

50. A. Shenhar, I. Gotmana, S. Radinb, P. Ducheyne, and E.Y. Gutmanas, Titanium Nitride Coatings on Surgical Titanium Alloys Produced by a Powder Immersion Reaction Assisted Coating Method: Residual Stresses and Fretting Behavior, *Surface Coat. Technology*, 2000, **126**, p 210–218. https://doi.org/10.1016/S0257-8972(00)00524-7

51. Y. Fu, H. Du, and Ch.Q. Sun, Interfacial Structure, Residual Stress and Adhesion of Diamond Coatings Deposited on Titanium, *Thin Solid Films*, 2003, **424**, p 107–114. https://doi.org/10.1016/S0040-6090(02)00908-2

52. G. Singh, S. Sharma, M. Mittal, G. Singh, J. Singh, L. Changhe, A.M. Khan, S.P. Dwivedi, R.T. Mushtaq, and S. Singh, Impact of Post-heat-treatment on the Surfaceroughness, Residual Stresses, and Micromorphology Characteristics of Plasmasprayed Pure Hydroxyapatite and 7%-Aloxite Reinforced Hydroxyapatite Coatings Deposited on Titanium Alloy-based Biomedical Implants, *J. Mater. Res. Technol.*, 2022, **18**, p 1358–1380. https://doi.org/10.1016/j.jmrt.2022.03.065

53. R. Singh, S. Schruefer, S. Wilson, J. Gibmeier, and R. Vassen, Influence of Coating Thickness on Residual Stress and Adhesion-strength of Cold-sprayed Inconel 718 Coatings, *Surf. Coat. Technol.*, 2018, **350**, p 64–73. https://doi.org/10.1016/j.surfcoat.2018.06.080

54. A. Vereschaka, M. Volosova, A. Chigarev, N. Sitnikov, A. Ashmarin, C. Sotova, J. Bublikov, and D. Lytkin, Influence of the Thickness of a Nanolayer Composite Coating on Values of Residual Stress and the Nature of Coating Wear, *Coatings*, 2020, **10**, p 63. https://doi.org/10.3390/coatings10010063

55. K. Khlifi, H. Dhiflaoui, Z. Lassaad, and A.B.C. Larbi, Mechanical Characterization of CrN/CrAlN Multilayer Coatings Deposited by Magnetron Sputtering System, *J. Mater. Eng. Perform.*, 2015, **24**, p 4077–4082. https://doi.org/10.1007/s11665-015-1692-x

56. M. Bielawski, Residual Stress Control in TiN/Si Coatings Deposited by Unbalanced Magnetron Sputtering, *Surf. Coat. Technol.*, 2006, **200**, p 3987–3995. https://doi.org/10.1016/j.surfcoat.2005.06.004

57. A. Ghasemi and S.A. Sadough Vanini, A Comprehensive Investigation on the Effect of Controlling Parameters of Ultrasonic Peening Treatment on Residual Stress and Surface Roughness: Experiments, Numerical Simulations and Optimization, *Surf. Coat. Technol.*, 2023, **464**, p 129515. https://doi.org/10.1016/j.surfcoat.2023.129515

58. F. Ahmed, M. Zain-ul-abdein, I.A. Channa, M.K. Yaseen, S.J. Gilani, M.A. Makhdoom, M. Mansoor, U. Shahzad, and M.N.B. Jumah, Effect of Ultrasonic Surface Mechanical Attrition Treatment-Induced Nano-grains on the Mechanical Properties and Biocompatibility of Pure Titanium, *Materials*, 2022, **15**, p 5097. https://doi.org/10.3390/ma15155097

59. S. Zhao, Y. Wang, L. Peng, Y.X. Zhang, R. Ran, and G. Yuan, Effect of Annealing Temperature on Microstructure and Mechanical Properties of Cold-rolled Commercially Pure Titanium Sheets, *Trans. Nonferrous Metals Soc. China*, 2022, **32**(8), p 2587–2597. https://doi.org/10.1016/S1003-6326(22)65968-5

60. R. Liu, S. Yuan, N. Lin, Z. Liu, Y. Yu, Z. Wang, Q. Zeng, W. Chen, L. Tian, L. Qin, B. Li, H. Zhang, Z. Wang, B. Tang, and Y. Wu, Tailoring Tribological Performance of Pure Titanium by a Duplex Treatment of Laser Surface Texturing-Thermal Oxidation, *J. Mater. Eng. Perform.*, 2020, **29**, p 4047–4062. https://doi.org/10.1007/s11665-020-04875-x

61. A.K. Pandey, A. Kumar, R. Kumar, R.K. Gautam, and C.K. Behera, Tribological Performance of SS 316L, Commercially Pure Titanium, and Ti6Al4V in Different Solutions for Biomedical Applications, *Mater. Today Proc.*, 2023, **78**(4), p A1–A8. https://doi.org/10.1016/j.matpr.2023.03.736

62. S. Wang, Q. An, W. Liu, R. Zhang, Z. Ma, L. Huang, and L. Geng, Towards Strength-ductility Enhancement of Titanium Matrix Composites through Heterogeneous Grain Structured Ti Matrix Design, *J. Alloy. Compd.*, 2022, **927**, p 167022. https://doi.org/10.1016/j.jallcom.2022.167022

63. S. Bajda, Y. Liu, R. Tosi, K. Cholewa-Kowalska, M. Krzyzanowski, M. Dziadek, M. Kopyscianski, S. Dymek, A.V. Polyakov, I.P. Semenova, and T. Tokarski, Laser Cladding of Bioactive Glass Coating on Pure Titanium Substrate with Highly Refined Grain Structure, *J. Mech. Behav. Biomed. Mater.*, 2021, **119**, p 104519. https://doi.org/10.1016/j.jmbbm.2021.104519

64. L. Morejón-Alonso, C. Mochales, L. Nascimento, and W.D. Müller, Electrochemical Deposition of Sr and Sr/Mg-co-substituted Hydroxyapatite on Ti-40Nb Alloy, *Mater. Lett.*, 2019, **248**, p 65–68. https://doi.org/10.1016/j.matlet.2019.03.141